RESEARCH ARTICLE

Check for updates

2D pyrene-based metal–organic framework nanobelts as efficient photocatalysts for the coupling of thiols into disulfides†

Xin Zhao,[a] Yajun Zhao,[a] Tao He,[c] Jing-Tong Deng,[c] Zong-Wen Mo [ID] [a] and Jiewei Liu [ID] *[a,b]

Photocatalytic coupling of thiols is a promising green approach to obtain disulfides. In this work, we report a stable pyrene-based MOF (Ni-PTTB) and its exfoliated two-dimensional (2D) nanobelts (Ni-PTTB-NB), which were prepared through the self-assembly of 1,3,6,8-tetrakis(3-carboxyphenyl) pyrene (H$_4$PTTB) and Ni(NO$_3$)$_2$·6H$_2$O. Taking advantages of the uniformly dispersed π-conjugated pyrene units, the obtained pyrene-based MOFs displayed visible-light absorption as well as intriguing optoelectronic properties. Interestingly, the 2D Ni-PTTB-NB showed obviously improved charge separation and migration compared to the pristine bulk Ni-PTTB, as revealed by a range of photoelectrochemical tests as well as Kelvin probe force microscopy (KPFM) measurements. Importantly, the Ni-PTTB-NB exhibited exceptional catalytic performance in the photocatalytic coupling of thiols in the air, giving rise to a 99% conversion of thiols and 99% selectivity of the disulfide products. Mechanism studies disclosed that the thiyl radicals are important intermediate in the catalytic process, which are obtained through the oxidation of thiols by the photogenerated holes. This work provides insights into the future design and development of 2D MOFs for the photocatalytic synthesis of high-value organic compounds.

Introduction

Disulfides are important synthetic intermediates, which are widely used in diverse fields, ranging from biochemistry to industrially important polymers.[1,2] The selective coupling of thiols is considered to be a feasible way to obtain disulfides.[3,4] However, massive methods for this coupling reaction usually require expensive/toxic reagents or harsh reaction conditions, as well as complicated purification processes, resulting in massive energy consumption and environmental pollution.[5,6] Thus, the synthesis of disulfides *via* heterogeneous photocatalytic routes would be meaningful from the standpoint of green and sustainable chemistry with broad application prospects. Although a few heterogeneous photocatalysts have been developed, the sophisticated reaction atmosphere (O$_2$ or inert

[a]School of Environmental and chemical Engineering, Jiangmen Key Laboratory of Synthetic Chemistry and Cleaner Production, Wuyi University, Jiangmen 529020, P.R. China. E-mail: wyuchemliujw@126.come
[b]Institute of Carbon Peaking and Carbon Neutralization, Wuyi University, Jiangmen 529020, P.R. China
[c]School of Pharmacy and Food Engineering, Wuyi University, Jiangmen 529020, P.R. China
†Electronic supplementary information (ESI) available. CCDC 2347068. For ESI and crystallographic data in CIF or other electronic format see DOI: https://doi.org/10.1039/d4qi01273a

gas) as well as the long reaction time (Table S1†) still remain key hurdles to the widespread applications.[7–15] Therefore, it would be of great significance to explore heterogeneous catalyst for the photocatalytic coupling of thiols with a facile operation route and satisfactory efficiency.

As an emerging class of porous materials composed of metal clusters and adjustable organic ligands, metal–organic frameworks (MOFs) provide a versatile platform for the rational design of heterogeneous photocatalysts.[16,17] Compared to 3D bulk MOFs, two-dimensional (2D) MOF nanosheets or nanobelts possess nanometre thickness to facilitate rapid mass transport as well as efficient photogenerated carrier transport, leading to improved photocatalytic activities.[18–21] As planar π-conjugation compounds, pyrene and its derivatives possess an electron-enriched skeleton as well as unique optical and photoelectronic properties, which enable them to be promising candidates for the design of photoactive MOFs.[22–24] The uniform structure of MOFs offers opportunities to heterogenize and isolate pyrene units in an ordered array, which renders pyrene-based MOFs with visible-light absorption, and rapid charge separation and transfer capabilities, giving rise to excellent photophysical and photochemical properties.[25] Currently, numerous works have focused on 3D pyrene-based MOFs for photocatalytic application;[26–28] however, the study of 2D pyrene-based MOFs in photocatalysis is still in its infancy and worth further exploration.[29–32]

5700 | *Inorg. Chem. Front.*, 2024, **11**, 5700–5708

This journal is © the Partner Organisations 2024

Herein, we report a new stable pyrene-based MOF, namely Ni-PTTB, consisting of the H_4PTTB ligand (H_4PTTB = 1,3,6,8-tetrakis(3-carboxyphenyl) pyrene) and a binuclear nickel–oxygen cluster. The 2D Ni-PTTB-NB was successfully prepared from the bulk Ni-PTTB crystal *via* a simple ultrasonic exfoliation process. The resulting 2D Ni-PTTB-NB exhibited significantly improved charge separation and migration, as confirmed by a series of photoelectrochemical studies. Meanwhile, Ni-PTTB-NB displayed remarkable photocatalytic performance towards the photocatalytic coupling of thiol in the air, giving rise to the corresponding disulfide with high selectivity.

Results and discussion

Synthesis and structural characterizations

The green rod-shaped crystals of Ni-PTTB were obtained through the solvothermal reaction of H_4PTTB with Ni$(NO_3)_2 \cdot 6H_2O$ in the presence of DMF and EtOH at 120 °C for 72 h (Fig. S1†). The FT-IR spectra of H_4PTTB and WYU-11 are displayed in Fig. S2.† Single-crystal X-ray diffraction analysis disclosed that Ni-TPPB adopted a 2D layered stacking mode, which crystallizes in the monoclinic with the space group $C2/m$. The asymmetric unit of Ni-PTTB consisted of one PTTB^{4-} ligand, two Ni^{2+} ions, and one coordinated water molecule. Each deprotonated PTTB ligand is coordinated with six Ni^{2+} ions *via* six O atoms, leaving two O atoms uncoordinated (Fig. 1a). It was interesting to note that the uncoordinated carboxyl oxygen atoms in the H_4PTTB ligand could serve as acid–base buffer sites, strengthening the stability of Ni-PTTB in aqueous solution.[30] In the binuclear nickel–oxygen cluster, Ni1 is coordinated with two O atoms from different H_4PTTB linkers and a bridging O atom, while Ni2 is connected with four O atoms from four different H_4PTTB linkers, and the length of Ni–O bonds are in the range of 2.04–2.09 Å (Fig. S3a†). Such coordination mode between Ni atoms and H_4PTTB linkers enables the formation of Ni-PTTB into two-dimensional (2D) sheets, meanwhile the adjacent single layers are stacked orderly, giving rise to a 3D structure with an inter-layer distance of 10 Å (Fig. 1b and S3b†). The three-dimensional (3D) framework exhibits a 1D irregular rectangle channel with a size of 10.3 × 9.1 Å^2 along the a-axis and an irregular hexagon channel with a cross-section of about 14.3 × 8.1 Å^2 along the c-axis (including the van der Waals radius of the atoms), respectively (Fig. S3c and S3d†). The 3D network of Ni-PTTB exhibits a (4,4)-connected **sql** topology with the point symbol of $\{4^4 \cdot 6^2\}$ (Fig. 1c). The powder X-ray diffraction (PXRD) patterns of Ni-PTTB were consistent with the simulated one, manifesting the good phase purity of the as-synthesized material (Fig. 1d). Scanning electron microscopy energy-dispersive X-ray spectroscopy (SEM-EDX) analysis verified the presence of all the constituent elements (C, O, Ni) in Ni-PTTB (Fig. S4†). The thermogravimetric (TG) curves of the activated samples disclosed the good thermal stability of Ni-PTTB, with a decomposition temperature up to 300 °C (Fig. S5†). The chemical stability of Ni-PTTB was tested by immersing the samples in various organic solvents and aqueous solution in the pH range of 2–12 for 5 days, respectively, and the unchanged PXRD patterns verified the samples' excellent stability (Fig. S6 and S7†).
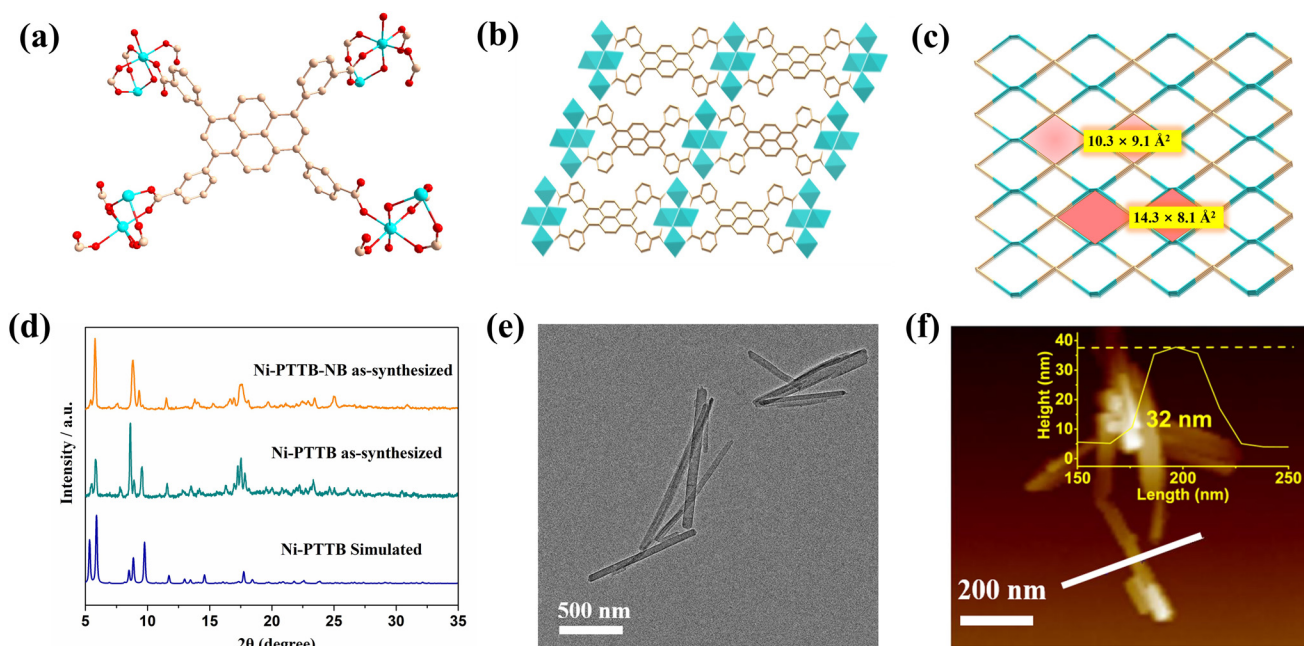

Fig. 1 (a) Characterization of Ni–PTTB and Ni–PTTB-NB. Coordination environment of the PTTB^{4-} ligand; (b) 2D layered structure viewed along the b-axis direction; (c) schematic representation of the (4,4)-connected framework of Ni-PTTB with the **sql** topology; (d) PXRD patterns; (e) TEM image of Ni-PTTB-NB; (f) atomic force microscopy (AFM) image of Ni-PTTB-NB (insert: height profile).

This journal is © the Partner Organisations 2024

Inorg. Chem. Front., 2024, **11**, 5700–5708 | **5701**

In light of the excellent stability of Ni-PTTB in organic solvents, bulk single crystals of Ni-PTTB were further treated in an ultrasonic ethanol solution for 30 min, leading to the formation of 2D Ni-PTTB nanobelts (denoted as Ni-PTTB-NB) (Fig. S8†). The well fitted PXRD patterns of Ni-PTTB-NB with that of the pristine Ni-PTTB suggested that its crystallinity could be well maintained during the simple ultrasonic exfoliation process (Fig. 1d). The morphology of the exfoliated Ni-PTTB-NB was revealed by scanning electron microscopy (SEM) and transmission electron microscopy (TEM), indicating that the exfoliated Ni-PTTB samples were thin strip-shaped structures about 900 nm length and 50 nm width (Fig. 1e and S9†). The thickness of Ni-PTTB-NB was measured to be 32 nm using atomic force microscopy (AFM) (Fig. 1f); therefore, the layer number of the obtained Ni-PTTB-NB was estimated to be 32, taking into account the theoretical interlayer distance of Ni-PTTB (Fig. S3b†). Such thin layers would provide more opportunities for close contact between the substrates and the active sites in the MOFs. The X-ray photoelectron spectroscopy (XPS) spectrum of Ni 2p exhibited two subpeaks, located at 856.2 and 874.2 eV, which could be assigned to Ni $2p_{3/2}$ and Ni $2p_{1/2}$, respectively (Fig. S10†). Meanwhile, two satellite peaks appeared simultaneously at 861.3 and 880.0 eV, respectively. The spin-energy separation of the two main peaks was around 18 eV, indicating the +2 valence nature of Ni in Ni-PTTB-NB.[33]

Photoelectrochemical properties

Ni-PTTB-NB exhibited broad absorption in the range of 300–800 nm in the solid-state UV-vis spectra (Fig. 2a). The band gap energy of Ni-PTTB-NB was calculated to be 2.76 eV according to the Tauc plot (Fig. 2a, insert). Mott–Schottky (M–S) measurements indicated the n-type semiconductor characteristics of Ni-PTTB-NB, and the flat band potential was determined to be −1.98 V (Fig. 2b). Therefore, the conduction band (CB) and valence band (VB) values of Ni-PTTB-NB were calculated to be −1.78 and 0.98 V, respectively, considering that the
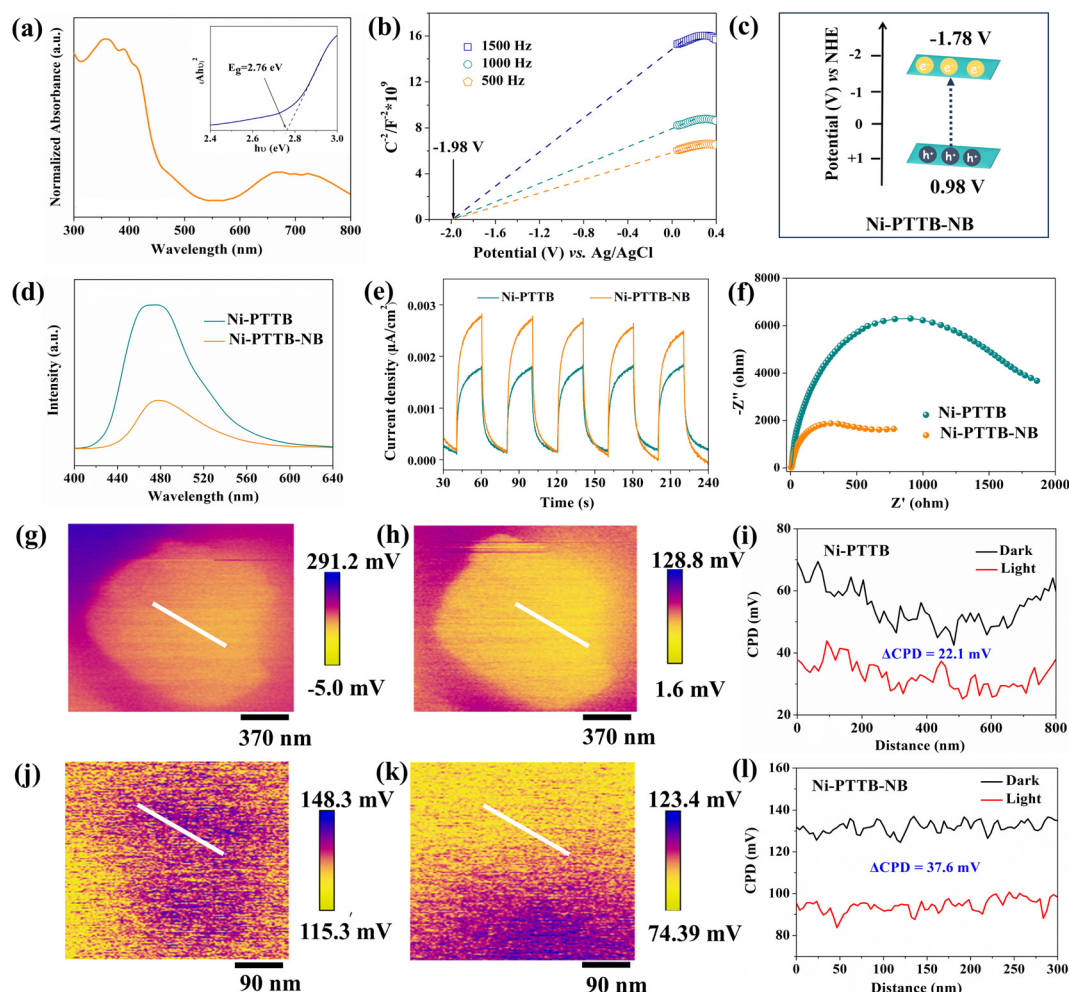
Fig. 2 (a) Solid-state UV-vis of Ni-PTTB-NB (insert: Tauc plot); (b) Mott–Schottky plot of Ni-PTTB-NB in 0.2 M Na$_2$SO$_4$ aqueous solution (pH 6.8); (c) band structures of Ni-PTTB-NB; PL spectra (d), transient photocurrent response (e) and Nyquist plots (f) of Ni-PTTB and Ni-PTTB-NB; KPFM images of Ni-PTTB in the dark (g) and under illumination (h); (i) corresponding line-scanning surface potential profile of Ni-PTTB in the absence and presence of light; KPFM images of Ni-PTTB-NB in the dark (j) and under illumination (k); (l) corresponding line-scanning surface potential profile of Ni-PTTB-NB in the absence and presence of light.

bottom of the CB in n-type semiconductors is approximately equal to the flat band potential.[34] The band structure of Ni-PTTB-NB is shown in Fig. 2c.

The charge separation and migration properties of the as-synthesized materials were investigated. Ni-PTTB-NB displayed significantly suppressed photoluminescence (PL) emission intensity compared to Ni-PTTB, suggesting that rapid charge transfer occurred after exfoliation (Fig. 2d). Further evidence of this was obtained from the photocurrent tests and electrochemical impedance spectroscopy (EIS) analysis. Ni-PTTB-NB showed a higher photocurrent density than Ni-PTTB, implying its higher charge-transfer efficiency (Fig. 2e). In addition, Ni-PTTB-NB displayed a smaller EIS radius, indicating its smaller charge-transfer resistance (Fig. 2f). We also carried out open-circuit potential (OCP) response measurements to identify the promoted charge separation over Ni-PTTB and Ni-PTTB-NB. The open-circuit potential (OCP) response reflects the electron-transfer process on a material surface, in which a decreased rate of OCP signals under a light-off condition indicates the lifetime of the photogenerated charge carriers.[35] As shown in Fig. S11,† Ni-PTTB-NB had a slower decreased rate than Ni-PTTB, suggesting that Ni-PTTB-NB has a relatively longer lifetime of charge carriers than Ni-PTTB. Combining the PL, photocurrent, EIS, and OCP measurements, it could be inferred that after exfoliation, the resulting Ni-PTTB-NB is beneficial for promoting the separation of photogenerated charge carriers, as well as improving the charge-carrier mobility.

To gain visual evidence of the charge-migration processes on the surfaces of Ni-PTTB and Ni-PTTB-NB, light-assisted Kelvin probe force microscopy (KPFM) measurements were carried out (Fig. 2g–l). When the sample comes into electrical contact with the Kelvin tip, the Fermi levels (E_f) of both would realign to arrive at equilibrium *via* the electron flow.[36] The contact potential difference (CPD) represents the difference in work function between the Kelvin tip (Φ_t) and the sample (Φ_s). As shown in Fig. 2g, h, j and k, the different colours reflect the diverse CPD values of the materials due to the differential E_f in the absence and presence of light. Under light irradiation, electron–hole pairs were photoexcited and separated, and afterwards a downward bending of E_f on the material surface or upward bending of the vacuum level (E_v) occurred, which would result in the decreased CPD values of the materials. The CPD variations along a straight line, both before and after visible irradiation using Ni-PTTB and Ni-PTTB-NB, are depicted in Fig. 2i and l respectively. It is generally accepted that the surface photovoltage can be determined by evaluating the contact potential difference (ΔCPD) in the absence and presence of light.[37,38] Since Ni-PTTB-NB exhibited a larger ΔCPD (37.6 mV) than that of Ni-PTTB (22.1 mV), it could be therefore concluded that the exfoliated Ni-PTTB-NB offers considerable improvements in the separation and migration of photogenerated charge carriers.

Photocatalytic coupling of thiols to disulfide

The excellent visible-light absorption, increased chance for intimate contact between the substrates and the framework,

and especially the enhanced charge-transfer properties of Ni-PTTB-NB, motivated us to explore its potential photocatalytic application. The synthesis of disulfides has aroused widespread attention nowadays as they are important intermediates in organic transformation and medicinal chemistry.[39] Initially, 4-methoxythiophenol (**1a**) was chosen as the model substrate. To our delight, Ni-PTTB-NB displayed high efficiency towards this reaction, giving rise to the corresponding bis(4-methoxyphenyl) disulfide (**2a**) product with a conversion of 99% and a selectivity of 99% under visible light ($\lambda > 400$ nm) irradiation for 2 h (Table 1, entry 1). In contrast, bulk Ni-PTTB exhibited a significantly decreased conversion (35%) (Table 1, entry 2). In order to clarify the activity of each component in Ni-PTTB-NB, control experiments were studied. When the ligand H$_4$PTTB was used as the catalyst, a 35% conversion of **1a** was obtained (Table 1, entry 3), while Ni(NO$_3$)$_2$ only gave a trace conversion of **1a** (Table 1, entry 4). In addition, no product could be detected with the catalyst-free system (Table 1, entry 5). Also, without visible light irradiation, this coupling reaction could hardly proceed (Table 1, entry 6). Furthermore, the reaction was carried out under N$_2$ atmosphere, and the unaffected catalytic activity ruled out the possibility that O$_2$ was involved in the photocatalytic process (Table 1, entry 7). We also conducted solvent optimization experiments, and the results showed that MeCN delivered the best performance (Table S4†).
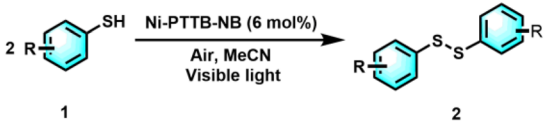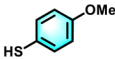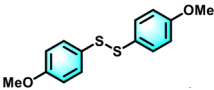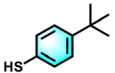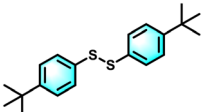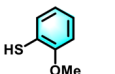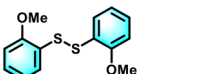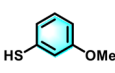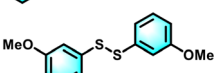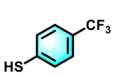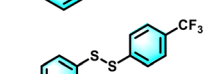
With the optimal reaction conditions established, the scope of the applicable thiols was examined, and it was found that a series of thiophenols bearing different substituent groups could smoothly transform into their corresponding disulfides with excellent conversion and selectivity (Table 2, entries 1–8). It was found that electron-donating groups (Table 2, entries 1–4) or electron-withdrawing groups on the benzene ring (Table 2, entries 5–8) could be well tolerated. In addition, *para*-, *meta*-, and *ortho*-substituted thiophenol derivatives exhibited

Table 1 Control experiments for the photocatalytic coupling of thiol[a]

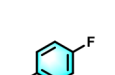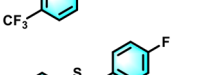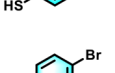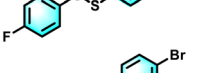| Entry	Catalyst	Conversion[b] (%)	Selectivity[c] (%)
1	Ni-PTTB-NB	99	99
2[d]	Ni-PTTB	37	99
3[e]	H$_4$PTTB	35	99
4[f]	Ni(NO$_3$)$_2$	4	99
5	—	0	0
6[g]	Ni-PTTB-NB	Trace	Trace
7[h]	Ni-PTTB-NB	99	99

[a] Reaction conditions: 4-methoxythiophenol (14 mg, 0.1 mmol), Ni-PTTB-NB (5.6 mg, 6 mol%), MeCN (5 mL), visible light ($\lambda > 400$ nm), 2 h. [b] The conversion of 4-methoxythiophenol was determined by gas chromatography (GC) using hexadecane as the internal standard. [c] The selectivity of the corresponding bis(4-methoxyphenyl) disulfide was determined by GC using hexadecane as an internal standard. [d] 6 mol% of Ni-PTTB. [e] 6 mol% of H$_4$PTTB. [f] 6 mol% of Ni(NO$_3$)$_2$. [g] Without visible light irradiation. [h] N$_2$ atmosphere.

Table 2 Photocatalytic coupling of various thiols catalyzed by Ni-PTTB-NB[a]

Entry	Substrate	Product	Conversion (%)[b]	Selectivity[c] (%)
1			99	99
2			99	99
3			99	99
4			99	99
5			99	99
6			99	99
7			99	99

[a] Reaction conditions: thiol (0.1 mmol), Ni-PTTB-NB (5.6 mg, 6 mol%), MeCN (5 mL), Visible light ($\lambda > 400$ nm), 2 h. [b] The conversion of thiol was determined by gas chromatography (GC) using hexadecane as an internal standard. [c] The selectivity of the corresponding disulfide was determined by GC using hexadecane as an internal standard.
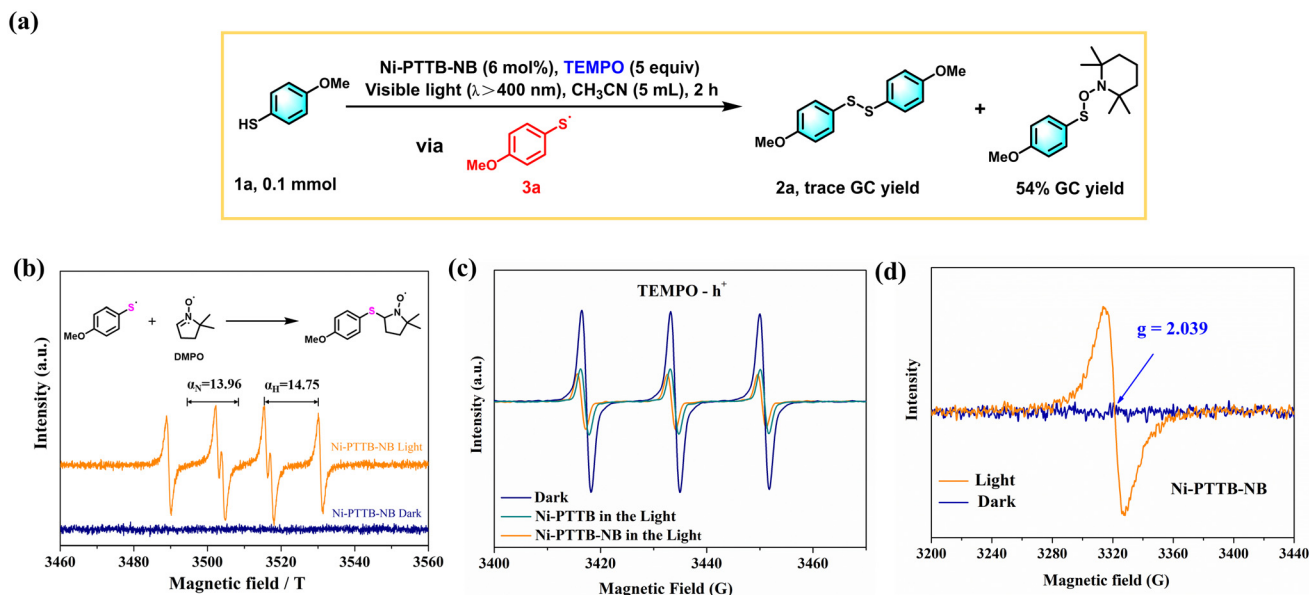
similar high activities (Table 2, entries 1, 3, and 4). Moreover, the generation rate of bis(4-methoxyphenyl) disulfide was calculated to be 8.9 mmol g h^{-1}, which was comparable to other heterogeneous catalysts (Fig. S1†).

Recyclability is an important parameter for heterogeneous catalysis. The recyclability of Ni-PTTB-NB was investigated. As shown in Fig. S12,† Ni-PTTB-NB could be recycled for up to 9 runs without loss of activity. The PXRD patterns of the recycled catalysts disclosed that the framework structure was retained but the crystallinity was poorer after photocatalysis (Fig. S13†). Meanwhile, the TEM image of the recycled Ni-PTTB-NB disclosed that its morphology was almost maintained the same (Fig. S14†). As indicated by the XPS spectra, the +2 valence state of Ni remained in the recycled photocatalyst (Fig. S15†). After the photocatalysis, the amount of Ni leaching into the reaction mixture was found to be 0.45%, as revealed by ICP-MS analysis of the filtrate.

Mechanism studies

To uncover the underlying reacting mechanism, a controlled experiment was performed to evaluate the active species in the photocatalytic process. 2,2,6,6-Tetramethylpiperidinooxy

(TEMPO), an effective radical trapping agent, was employed to capture the thiyl radical.[40] The addition of TEMPO to the catalytic mixture significantly inhibited the conversion of 4-methoxythiophenol (**1a**), giving rise to only a trace amount of bis(4-methoxyphenyl) disulfide (**2a**) (Fig. 3a). We also carried out electron paramagnetic resonance (EPR) measurements using 5,5-dimethyl-1-pyrrolin N-oxide (DMPO) as the trapping agent to detect the intermediate radical in the photocatalytic coupling of thiols. As shown in Fig. 3b, no characteristic signal peaks were observed in the dark; whereas under light illumination, Ni-PTTB-NB exhibited six characteristic signal peaks associated with thiyl radical intermediates ($\alpha_N = 13.96$ and $\alpha_H = 14.75$, related to the nitrogen hyperfine splitting and hydrogen hyperfine splitting of the nitroxide nitrogen), verifying the production of thiyl radicals during the photocatalytic process.[11,41,42] The above EPR results disclosed that light irradiation is a precondition to generate thiyl radicals, which thus further promote the photocatalytic performance. Meanwhile, the thiyl-TEMPO adduct was detected by GC-MS (Fig. S16†), which also confirms the fact that the thiyl radical (**3a**) was generated during the photocatalytic process. Since the oxidation potential of **1a** is reported to be 0.35 vs. NHE,[42] and

5704 | *Inorg. Chem. Front.*, 2024, **11**, 5700–5708

This journal is © the Partner Organisations 2024

(a)

(b)

(c)

(d)

Fig. 3 (a) Trapping of thiyl radicals; (b) EPR spectrum of capturing thiyl radicals over Ni-PTTB-NB; (c) EPR spectra of TEMPO-h$^+$ over Ni-PTTB and Ni-PTTB-NB; (d) EPR spectra of Ni-PTTB-NB, manifesting the formation of Ni$^+$ during photocatalysis.

the VB of Ni-PTTB-NB is 0.98 V *vs.* NHE, which is more positive than the oxidation potential of **1a**, therefore it is thermodynamically feasible for the oxidation of **1a** to the corresponding thiyl radical (**3a**) over Ni-PTTB-NB.

To further investigate the oxidation process, TEMPO was used as a spin-trapping agent for detecting photogenerated holes (h$^+$).[43] In the dark, a 1 : 1 : 1 triplet spectrum was clearly observed, which is the characteristic peak of TEMPO.[44] Under visible-light irradiation, the peak signal became weak due to the consumption of TEMPO and the formation of the TEMPO-h$^+$ adduct, demonstrating the generation of h$^+$. It was found that the EPR signal in Ni-PTTB-NB was weaker than that of Ni-PTTB (Fig. 3c), suggesting more holes were generated over Ni-PTTB-NB, which is in accordance with the above analysis. The photogenerated holes would participate in the oxidation of **1a**. Thus, electron transfer within Ni-PTTB-NB was also studied. As shown in Fig. 3d, an obvious signal peak with a g value of 2.039 occurred under light irradiation, with the observation of this signal indicating the formation of paramagnetic Ni(I) species,[45] due to the reduction of Ni^{2+} into Ni$^+$ during the photocatalysis. According to the EPR experiment results, a ligand-to-metal charge-transfer (LMCT) process occurred in Ni-PTTB, whereby the photoexcited electrons transfer from the excited PTTB group to the binuclear nickel–oxygen cluster, resulting in the reduced Ni(I) species.

Based on the above discussion, a possible mechanism is proposed and illustrated in Fig. 4. Prior to the photocatalysis, the thiol substrates would be adsorbed onto the surface of Ni-PTTB-NB at the initial stage. Under light irradiation, the H$_4$PTTB ligand would behave as an effective visible light harvester to capture photons, and then the Ni-PTTB-NB is photoexcited to generate charge carriers. Photogenerated electrons
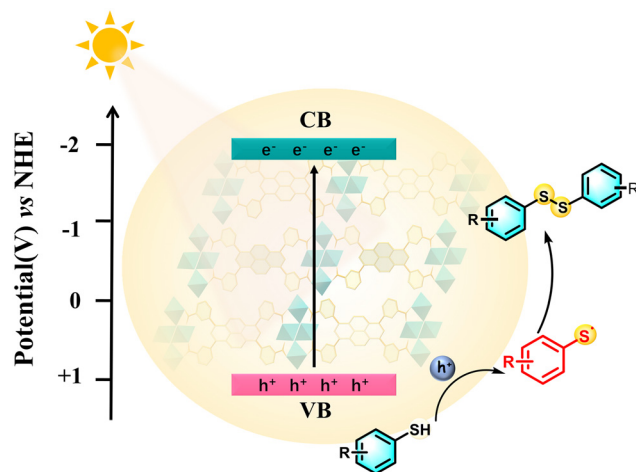
Fig. 4 Systematic illustration of the mechanism for the photocatalytic coupling of thiols to disulfide over Ni-PTTB-NB ($\lambda > 400$ nm).

(e$^-$) and h$^+$ are generated on the CB and VB of Ni-PTTB-NB, respectively. Subsequently, the thiol substrate is oxidized by the photogenerated h$^+$, leading to the formation of thiyl radical intermediates. Finally, the thiyl radical intermediates would couple with each other to afford the corresponding disulfide products with high selectivity.

Conclusion

In summary, we successfully synthesized a 2D pyrene-based MOF nanobelt (Ni-PTTB-NB), which showed excellent activities

This journal is © the Partner Organisations 2024

Inorg. Chem. Front., 2024, **11**, 5700–5708 | **5705**

in the photocatalytic coupling of thiols to obtain high-value disulfides in the air. The enhanced charge separation and migration in Ni-PTTB-NB compared to the 3D bulk Ni-PTTB was studied in detail. The generated thiyl radicals and photo-generated holes were demonstrated to play important roles in the photocatalytic process. A possible mechanism was proposed for the photocatalytic coupling of thiols to disulfide. The present work provides guidance on the rational design and fabrication of 2D MOFs towards the photocatalytic synthesis of high-value chemicals. Further work on the design and application of pyrene-based MOFs in photocatalytic applications is in progress.

Experimental section

Synthesis of Ni-PTTB

H_4PTTB (12.3 mg, 0.018 mmol), $Ni(NO_3)_2 \cdot 6H_2O$ (29 mg, 0.1 mmol), diethylformamide (DEF, 3.5 mL), and H_2O (1 mL) were placed into a glass vial. The mixture was heated at 120 °C for 72 h and then cooled to room temperature at a rate of 5 °C h^{-1}. The green rod-shaped crystals of Ni-PTTB were harvested (13 mg, 88.2% yield based on H_4PTTB), and washed with acetone three times and then dried at room temperature. Anal Calcd For $[Ni_2(PTTB)] \cdot 3DEF \cdot 14H_2O$ ($C_{59}H_{87}N_3Ni_2O_{25}$): C, 52.27; H, 6.47; N, 3.10%. Found: C, 52.27; H, 5.81%; N, 3.96%. FT-IR (KBr) ν 3430 (w), 1646 (m), 1396 (s), and 1118 (m) cm^{-1}.

Synthesis of Ni-PTTB-NB nanobelts

First, 100 mg of the Ni-PTTB sample was subjected to ultrasonic treatment in 100 mL ethanol solution for 30 min, giving rise to a green suspension. Subsequently, the obtained Ni-PTTB-NB nanobelts were collected (92.3 mg, 92.3% yield) by centrifugation and dried overnight at 60 °C.

Photocatalytic thiol coupling reaction

Typically, 4-methoxythiophenol (**1a**, 14 mg, 0.1 mmol) and activated Ni-PTTB-NB (5.6 mg, 6 mol%) were stirred in CH_3CN (5 mL) under air and visible light irradiation ($\lambda > 400$ nm) for 2 h. After completion of the reaction, the catalyst was recycled by centrifugation and filtration, giving rise to the liquid phase. Then, hexadecane was added as an internal standard into the liquid phase, and the whole mixture was stirred for 5 min for the following GC analysis. The conversion of the thiol and the disulfide product selectivity were determined by GC (Agilent 8890 GC System chromatograph equipped with an FID detector). The calculations for thiol conversion and disulfide selectivity were as follows:

$$\text{Thiols conversion (\%)} = \frac{\text{Molar of reacted thiols}}{\text{Molar of initial thiols}} \times 100\%$$

$$\text{Disulfide product selectivity (\%)} = \frac{\text{Molar of disulfide product}}{\text{Molar of total product}} \times 100\%$$

Author contributions

The manuscript was written through contributions of all authors. X. Zhao performed the experiments, collected and analyzed the data. Y. Zhao, T. He and J.-T. Deng assisted the experiments. Z.-W. Mo analyzed the data. J. Liu conceived, designed the experiments and wrote the paper. All authors have approved the final version of the manuscript.

Data availability

The data supporting this article have been included as part of the ESI.†

Conflicts of interest

There are no conflicts to declare.

Acknowledgements

References

1 L. Li, Z. Li, A. Yoshimura, C. Sun, T. Wang, Y. Chen, Z. Chen, A. Littlejohn, Y. Xiang, P. Hundekar, S. F. Bartolucci, J. Shi, S.-F. Shi, V. Meunier, G.-C. Wang and N. Koratkar, Vanadium disulfide flakes with nano-layered titanium disulfide coating as cathode materials in lithium-ion batteries, *Nat. Commun.*, 2019, **10**, 1764.

2 D. Fass and C. Thorpe, Chemistry and Enzymology of Disulfide Cross-Linking in Proteins, *Chem. Rev.*, 2018, **118**, 1169–1198.

3 M. Arisawa, K. Fukumoto and M. Yamaguchi, Rhodium-Catalyzed Oxidation of Unprotected Peptide Thiols to Disulfides with Oxygen in Water, *ACS Catal.*, 2020, **10**, 15060–15064.

4 H. Xu, Y.-F. Zhang and X. Lang, TEMPO visible light photocatalysis: The selective aerobic oxidation of thiols to disulfides, *Chin. Chem. Lett.*, 2020, **31**, 1520–1524.

5 C. Zhu, D. Wu, H. Liu, C. Mengb and T. Tang, Transformation of thiols to disulfides via an oxidant-free radical pathway on the zeolite ETS-10, *Green Chem.*, 2022, **24**, 9033–9039.

6 M. Oba, K. Tanaka, K. Nishiyama and W. Ando, Aerobic Oxidation of Thiols to Disulfides Catalyzed by Diaryl Tellurides under Photosensitized Conditions, *J. Org. Chem.*, 2011, **76**, 4173–4177.

5706 | *Inorg. Chem. Front.*, 2024, **11**, 5700–5708

This journal is © the Partner Organisations 2024

7 H. Wei, X. Li, F. Huang, S. Wu, H. Ding, Q. Chen, M. Li and X. Lang, Red light-driven generation of reactive oxygen species for the targeted oxidation of glioma cells and thiols over covalent organic framework, *Chin. Chem. Lett.*, 2023, **34**, 108564.

8 X. Dong, H. Hao, F. Zhang and X. Lang, Combining Brønsted base and photocatalysis into conjugated microporous polymers: Visible light-induced oxidation of thiols into disulfides with oxygen, *J. Colloid Interface Sci.*, 2022, **622**, 1045–1053.

9 H. Xu, J.-L. Shi, S. Lyu and X. Lang, Visible-light photocatalytic selective aerobic oxidation of thiols to disulfides on anatase TiO_2, *Chin. J. Catal.*, 2020, **41**, 1468–1473.

10 X.-J. Li, M.-Y. Qi, J.-Y. Li, C.-L. Tan, Z.-R. Tang and Y.-J. Xu, Visible light–driven dehydrocoupling of thiols to disulfides and H_2 evolution over PdS–decorated $ZnIn_2S_4$ composites, *Chin. J. Catal.*, 2023, **51**, 55–65.

11 M.-H. Sun, M.-Y. Qi, Z.-R. Tang and Y.-J. Xu, Dual cocatalysts decorated CdS nanoparticles for efficient dehydrocoupling of thiols into disulfides, *Appl. Catal., B*, 2023, **321**, 122019.

12 L. Xu, X. Deng and Z. Li, Photocatalytic splitting of thiols to produce disulfides and hydrogen over PtS/$ZnIn_2S_4$ nanocomposites under visible light, *Appl. Catal., B*, 2018, **234**, 50–55.

13 S. Shi, H. Li, Y. Zhang, Y. Shi, N. Zhang, T. Li, Y. Zhang, Q. Li, P. Duan and Y. Li, Photocatalytic hydrogen evolution and simultaneously converting high-concentration of thiols into disulfides with excellent yield under visible-light, *J. Mater. Chem. A*, 2023, **11**, 2726–2736.

14 F. Su, C. Yang, Z. Wang, W. Zhao, H. Xie, S. Zhang, X. Jin, Q. Huang and L. Ye, Visible Light-Driven Photocatalytic Transformation of Thiols to Disulfides in Water Catalyzed by Bi_2S_3, *Adv. Energy Sustainability Res.*, 2023, **4**, 2300071.

15 X.-B. Li, Z.-J. Li, Y.-J. Gao, Q.-Y. Meng, S. Yu, R. G. Weiss, C.-H. Tung and L.-Z. Wu, Mechanistic Insights into the Interface-Directed Transformation of Thiols into Disulfides and Molecular Hydrogen by Visible-Light Irradiation of Quantum Dots, *Angew. Chem., Int. Ed.*, 2014, **53**, 2085–2089.

16 K. Sun, Y. Qian and H.-L. Jiang, Metal-Organic Frameworks for Photocatalytic Water Splitting and CO_2 Reduction, *Angew. Chem., Int. Ed.*, 2023, **62**, e202217565.

17 P. Rassu, X. Ma and B. Wang, Engineering of catalytically active sites in photoactive metal–organic frameworks, *Coord. Chem. Rev.*, 2022, **465**, 214561.

18 Y. Xue, G. Zhao, R. Yang, F. Chu, J. Chen, L. Wang and X. Huang, 2D metal–organic framework-based materials for electrocatalytic, photocatalytic and thermocatalytic applications, *Nanoscale*, 2021, **13**, 3911.

19 G. Chakraborty, I.-H. Park, R. Medishetty and J. J. Vittal, Two-Dimensional Metal-Organic Framework Materials: Synthesis, Structures, Properties and Applications, *Chem. Rev.*, 2021, **121**, 3751–3891.

20 M. Zhao, Y. Huang, Y. Peng, Z. Huang, Q. Ma and H. Zhang, Two-dimensional metal-organic framework nanosheets: synthesis and applications, *Chem. Soc. Rev.*, 2018, **47**, 6267.

21 Y. Fan, H. Zheng, S. Labalme and W. Lin, Molecular Engineering of Metal-Organic Layers for Sustainable Tandem and Synergistic Photocatalysis, *J. Am. Chem. Soc.*, 2023, **145**, 4158–4165.

22 J. Yu, J. Park, A. V. Wyk, G. Rumbles and P. Deria, Excited-State Electronic Properties in Zr-Based Metal-Organic Frameworks as a Function of a Topological Network, *J. Am. Chem. Soc.*, 2018, **140**, 10488–10496.

23 X. Dong, H. Zhao, K. Zhang and X. Lang, Pyrene-based porous organic materials for visible light photocatalysis, *Coord. Chem. Rev.*, 2024, **513**, 215902.

24 F. P. Kinik, A. Ortega-Guerrero, D. Ongari, C. P. Ireland and B. Smit, Pyrene-based metal organic frameworks: from synthesis to applications, *Chem. Soc. Rev.*, 2021, **50**, 3143.

25 X. Li, J. Yu, Z. Lu, J. Duan, H. C. Fry, D. J. Gosztola, K. Maindan, S. S. Rajasree and P. Deria, Photoinduced Charge Transfer with a Small Driving Force Facilitated by Exciplex-like Complex Formation in Metal-Organic Frameworks, *J. Am. Chem. Soc.*, 2021, **143**, 15286–15297.

26 A. Cadiau, N. Kolobov, S. Srinivasan, M. G. Goesten, H. Haspel, A. V. Bavykina, M. R. Tchalala, P. Maity, A. Goryachev, A. S. Poryvaev, M. Eddaoudi, M. V. Fedin, O. F. Mohammed and J. Gascon, A Titanium Metal-Organic Framework with Visible-Light-Responsive Photocatalytic Activity, *Angew. Chem., Int. Ed.*, 2020, **59**, 13468–13472.

27 Y. Zhang, J. Pang, J. Li, X. Yang, M. Feng, P. Caia and H.-C. Zhou, Visible-light harvesting pyrene-based MOFs as efficient ROS generators, *Chem. Sci.*, 2019, **10**, 8455.

28 Y. Xiao, X. Guo, J. Liu, L. Liu, F. Zhang and C. Li, Development of a bismuth-based metal-organic framework for photocatalytic hydrogen production, *Chin. J. Catal.*, 2019, **40**, 1339–1344.

29 Y. Xiao, Y. Qi, X. Wang, X. Wang, F. Zhang and C. Li, Visible-Light-Responsive 2D Cadmium-Organic Framework Single Crystals with Dual Functions of Water Reduction and Oxidation, *Adv. Mater.*, 2018, **30**, 1803401.

30 Y. Xiao, J. Liu, J. Leng, Z. Yin, Y. Yin, F. Zhang, C. Sun and S. Jin, Long-Lived Internal Charge-Separated State in Two-Dimensional Metal–Organic Frameworks Improving Photocatalytic Performance, *ACS Energy Lett.*, 2022, **7**, 2323–2330.

31 L. Liu, S. Du, X. Guo, Y. Xiao, Z. Yin, N. Yang, Y. Bao, X. Zhu, S. Jin, Z. Feng and F. Zhang, Water-Stable Nickel Metal-Organic Framework Nanobelts for Cocatalyst-Free Photocatalytic Water Splitting to Produce Hydrogen, *J. Am. Chem. Soc.*, 2022, **144**, 2747–2754.

32 D. He, Q. Wang, Y. Rong, Z. Xin, J.-J. Liu, Q. Li, K. Shen and Y. Chen, Sub-Nanometer Mono-Layered Metal-Organic Frameworks Nanosheets for Simulated Flue Gas Photoreduction, *Adv. Mater.*, 2024, 2403920.

33 P. Chakrabortty, S. Ghosh, A. Das, D. Khurana, T. S. Khan and S. M. Islam, Visible Light-Driven $C(sp^3)$-H Carboxylation of Diverse Amines with CO_2 into α-Amino Acids Using an Eco-Friendly and Reusable Covalent Organic Framework, *ACS Sustainable Chem. Eng.*, 2023, **11**, 8736–8752.

This journal is © the Partner Organisations 2024

Inorg. Chem. Front., 2024, **11**, 5700–5708 | **5707**

34 E.-Z. Deng, Y.-Z. Fan, H.-P. Wang, Y. Li, C. Peng and J. Liu, Engineering a Z-Scheme Heterostructure on $ZnIn_2S_4$@NH_2-MIL-125 Composites for Boosting the Photocatalytic Performance, *Inorg. Chem.*, 2024, **63**, 1449–1461.

35 D. Li, S.-H. Yu and H.-L. Jiang, From UV to Near-Infrared Light-Responsive Metal–Organic Framework Composites: Plasmon and Upconversion Enhanced Photocatalysis, *Adv. Mater.*, 2018, **30**, 1707377.

36 J. Cheng, S. Wan and S. Cao, Promoting Solar-driven Hydrogen Peroxide Production over Thiazole-based Conjugated Polymers via Generating and Converting Singlet Oxygen, *Angew. Chem., Int. Ed.*, 2023, **62**, e202310476.

37 Y. Guo, J. Sun, Y. Tang, X. Jia, Y. Nie, Z. Geng, C. Wang, J. Zhang, X. Tan, D. Zhong, J. Ye and T. Yu, Efficient interfacial electron transfer induced by hollow-structured $ZnIn_2S_4$ for extending hot electron lifetimes, *Energy Environ. Sci.*, 2023, **16**, 3462–3473.

38 Y. Ai, J. Hu, X. Xiong, S. A. C. Carabineiro, Y. Li, N. Sirotkin, A. Agafonov and K. Lv, Synergistic interfacial engineering of a S-scheme ZnO/In_2S_3 photocatalyst with S-O covalent bonds: A dual-functional advancement for tetracycline hydrochloride degradation and H_2 evolution, *Appl. Catal., B*, 2024, **353**, 124098.

39 N. Spiliopoulou and C. G. Kokotos, Photochemical metal-free aerobic oxidation of thiols to disulfides, *Green Chem.*, 2021, **23**, 546–551.

40 Y. Yuan, Y. Chen, S. Tang, Z. Huang and A. Lei, Electrochemical oxidative oxysulfenylation and aminosulfenylation of alkenes with hydrogen evolution, *Sci. Adv.*, 2018, **4**, eaat5312.

41 M. Jiang, H. Li, H. Yang and H. Fu, Room-Temperature Arylation of Thiols: Breakthrough with Aryl Chlorides, *Angew. Chem., Int. Ed.*, 2017, **56**, 874–879.

42 X.-J. Li, M.-Y. Qi, J.-Y. Li, C.-L. Tan, Z.-R. Tang and Y.-J. Xu, Visible light–driven dehydrocoupling of thiols to disulfides and H_2 evolution over PdS–decorated $ZnIn_2S_4$ composites, *Chin. J. Catal.*, 2023, **51**, 55–65.

43 S. Zhou, L. Jiang, H. Wang, J. Yang, X. Yuan, H. Wang, J. Liang, X. Li, H. Li and Y. Bu, Oxygen Vacancies Modified TiO_2/O-Terminated Ti_3C_2 Composites: Unravelling the Dual Effects between Oxygen Vacancy and High-Work-Function Titanium Carbide, *Adv. Funct. Mater.*, 2023, 2307702.

44 F. Huang, Y. Wang, X. Dong and X. Lang, Merging benzotrithiophene covalent organic framework photocatalysis with TEMPO for selective oxidation of organic sulfides, *Sci. China: Chem.*, 2023, **66**, 3290–3296.

45 J. Xu, R. Wang, L. Zheng, J. Ma, W. Yan, X. Yang, J. Wang, X. Su and Y. Huang, Unraveling the real active sites of an amorphous silica-alumina-supported nickel catalyst for highly efficient ethylene oligomerization, *Catal. Sci. Technol.*, 2021, **11**, 1510–1518.

5708 | *Inorg. Chem. Front.*, 2024, **11**, 5700–5708

This journal is © the Partner Organisations 2024